ADVANCED ENGINEERING MATERIALS
www.aem-journal.com

Micro-CT Analysis of Implanted Poly-Ether-Ether-Ketone Scaffolds: Plasma Immersion Ion Implantation Increases Osteoconduction

Georgio Katsifis, Hedi Kruse, Will Lewin, Abdullah Al Maruf, Jonathan R. Clark, David R McKenzie,* and Natalka Suchowerska*

Poly-ether-ether-ketone (PEEK) is a biocompatible, high-strength polymer with biomechanical properties similar to soft bone that has been proposed as an alternative to titanium for orthopedic implants. Herein, micro-CT imaging of a 3D printed PEEK scaffold treated with plasma immersion ion implantation (PIII) to assess the degree of osteoconduction relative to an identical untreated structure, by implantation in the scapula of sheep, is performed. To overcome the lack of contrast between soft tissue and PEEK, a customized apparatus and alignment technique is designed and constructed. Principal component analysis is used to accurately locate the boundaries of the implant in the 3D dataset, with respect to reference coordinates. It is found that, within the interior volume of the scaffold, the PIII treated PEEK contains bone that is both more dense and in higher amounts than for untreated PEEK. The untreated PEEK shows more bone immediately outside the boundaries of the scaffold, indicating a lower affinity of the untreated scaffold for in-diffusion of osteocytes and associated mineralization. The greater osteoconduction of the PIII treated scaffold is attributed to the improvement in hydrophilicity and the provision of protein covalent binding.

1. Introduction

Bone diseases such as osteosarcoma often require aggressive removal of bony tissue.[1] After surgery, bone function is restored by the hemostatic stimulation of the local bone to fill the defect.[2] In critical-sized defects, this mechanism is insufficient to fill bone loss and reconstruction using a bone graft from another part of the skeleton or a prosthetic bone implant is needed.[3,4] Titanium plates have been used to bridge bone segments but because of the differences in elastic modulus, implant failure from stress-shielding osteolysis may ultimately occur.[5–7] For cancer patients requiring radiation therapy, titanium causes unwanted shielding and scattering of the radiation, compromising treatment quality.[5,8–10] Poly-ether-ether-ketone (PEEK) is a thermoplastic polymer, with biomechanical properties similar to those of bone, and has been proposed as an alternative to titanium for implants, causing less interference for both imaging

G. Katsifis, H. Kruse, D. R. McKenzie, N. Suchowerska
School of Physics
The University of Sydney
Camperdown, NSW 2006, Australia
E-mail: gkat2146@uni.sydney.edu.au; david.mckenzie@sydney.edu.au

G. Katsifis, H. Kruse, W. Lewin, D. R. McKenzie, N. Suchowerska
VectorLAB
School of Physics
The University of Sydney
Camperdown, NSW 2006, Australia

H. Kruse, W. Lewin, J. R. Clark, D. R. McKenzie
Biomedical Innovation
Chris O'Brien Lifehouse
Missenden Rd, Camperdown, Sydney, NSW 2050, Australia

The ORCID identification number(s) for the author(s) of this article can be found under https://doi.org/10.1002/adem.202201297.

DOI: 10.1002/adem.202201297

H. Kruse
Royal Prince Alfred Institute of Academic Surgery
Sydney Local Health District
Missenden Road, Camperdown, NSW 2050, Australia

H. Kruse, W. Lewin, D. R. McKenzie
Sarcoma and Surgical Research Centre
Chris O'Brien Lifehouse
Missenden Rd, Camperdown, Sydney, NSW 2050, Australia

A. Al Maruf, J. R. Clark
Sydney Head and Neck Cancer Institute
Department of Head and Neck Surgery
Chris O'Brien Lifehouse
Missenden Rd, Camperdown, Sydney, NSW 2050, Australia

A. Al Maruf, J. R. Clark
Sydney Medical School
Faculty of Medicine and Health Sciences
The University of Sydney
Camperdown, NSW 2006, Australia

and radiation therapy.[5,8,11,12] PEEK is chemically inert but in its natural state has hydrophobic characteristics[5,13] that may prevent osseointegration.[14,15] Plasma immersion ion implantation (PIII) is a surface modification technique, which utilizes high ion energy bombardment to impart hydrophilic properties and provides reactive sites in carbon-based polymers, and allows better adhesion of bone on-growth and encouraging stronger binding of biomolecules, for example, bone morphogenic proteins that may assist bone growth.[14,16–18]

PIII has been demonstrated to be successful in treating the internal cavities of porous polymer objects with complex geometries.[16] The treatment has been found to remain active for long periods from months to years.[16,19] PIII treatment has been shown to promote calcium mineralization in vitro and to increase the proliferation of bone cells on polymer surfaces[14,20] by covalently binding biomolecules to the surface.[21] Using in vivo scapular implants in sheep, a stronger interface between the implant that had received PIII treatment and the bone of the host was demonstrated using a torque test.[22] However, it was not known from the previous study whether PIII could improve the penetration of bone mineralization into the cavities of a porous bone scaffold referred to here as osteoconduction.

The aim of the current study is to determine using micro-CT (μCT) whether PIII treatment provides improved osteoconduction of the scaffold as assessed by the extent of ingrowth of new bone into the scaffold implanted in the same sheep model. μCT is capable of determining the relative X-ray attenuation as a function of position in a specimen in Hounsfield units (HU), providing direct evidence of bone mineralization and osteoconduction.[23] However, this technique relies on adequate contrast between the phases which is influenced by the energy spectrum of the X-ray beam, the exposure, and the difference in attenuation between the phases.[5,6] Following integration with the body, outlining the boundaries of a PEEK scaffold can prove difficult because the X-ray attenuation properties of prebone tissues are very close to those of PEEK.[11,24] Here, we use innovative approaches to improve both data collection and data analysis to investigate the osteoconduction in the PEEK scaffold after implantation in the sheep.

Data analysis using simple thresholding and boundary detection is not adequate in cases where there is poor contrast between soft tissues. The noise and high scatter from higher density and atomic number materials[5] leads to overlap between the distribution of HU for soft tissue and PEEK and creates uncertainty in the thresholding.[25] Furthermore, traditional noise reduction techniques such as median filters or low pass filters are not always adequate as they may remove high-frequency components of the image that may be the result of tiny, isolated bone depositions.[5,26]

To improve data collection, we carried out careful alignment of the scaffold with the imaging axis by designing and constructing a novel immobilization device in polylactic acid (PLA), using fused deposition modeling (FDM), to fix the implant relative to the imaging bed during the acquisition of data. Iron PLA (FePLA) (55% PLA, <45% iron) rings and markers were utilized to locate the midpoint of the scaffold, and then, using principal component analysis (PCA), the angle of deviation was determined from the dot product of the unit vector along the z-axis and the principal component vector.[27]

2. Experimental Section

2.1. Design of Scaffold and μCT Stage

The scaffolds and μCT stage were designed using Fusion 360 (software version V.2.0.9719) and fabricated using fused deposition modeling in an AON M.2 3D printer [AON, Montreal, Canada]. The mesh portion of the implant consisted of a stack of alternating lattices of PEEK. The lattices were stacked in the Z direction such that each lattice would align with the printing plane during 3D printing by FDM. Each lattice consisted of a repeating pattern of a layer of rectilinear bars in the X direction, a layer of concentric rings, a layer of rectilinear bars in the Y direction, and a final layer of concentric rings. The parameters of the mesh scaffold were selected to achieve a structure that had an approximate porosity of 50% and was accurately producible in the printer; the width of the bars and gaps in the lattice was 0.5 mm, equal to the extrusion width during printing; and the height of the bars was 0.4 mm.

2.2. Sheep Model and Surgery

The 3×2.8 mm screw fixation holes were evenly distributed around the mesh center at a radius 14.3 mm. The holes were designed to fix the surface of the scaffold to the bone when implanted. Each of the three shapes of the fixation legs was designed with a unique shape to record the orientation of the scaffold when implanted. The scaffolds were implanted into the left scapula of the sheep, as shown in **Figure 1**. The pattern was designed differently for PIII treated implants compared to UT implants to distinguish treated from UT scaffolds. The design of the scaffold and the two primary layers of its microstructure are shown in **Figure 2**a–c.

In this study, half of the PEEK implant scaffolds were PIII treated and half were UT. A total of six sheep were implanted with the UT/PIII pairs and at 8, 10, and 12 weeks postsurgery, the sheep were sacrificed and implants were extracted. There were two sheep for each time point. Prior to implantation, the scaffolds were autoclaved at 134 °C using the standard cycle time of 4 min.

2.3. PIII

PIII utilizes high energy ions to modify the properties of a material.[28] In this work, the scaffold is capacitively coupled to a high voltage pulsed power supply as performed by Tran et al. and Katsifis et al.[16,29] Recently, the technique has gained popularity in the treatment of porous materials in the biomedical field as it is a nonline of sight technique and can treat small cavities as long as the plasma parameters are tuned appropriately.[29,30]

Twelve FDM printed PEEK scaffolds of each design were fabricated. Half of all the implants were treated with PIII using 10 kV negative square wave pulses at 1 kHz, with a length of 40 μs and rise time of 220 ns created by a RUP 6 (KE

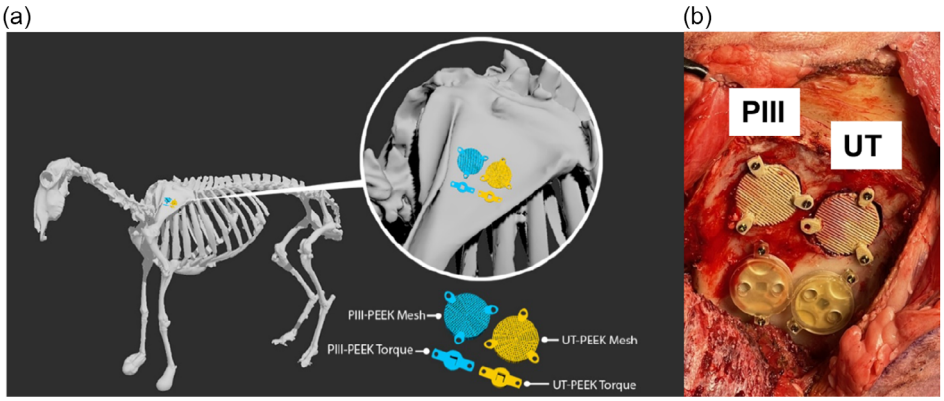

Figure 1. Surgical location of the ion implanted (PIII) treated (blue) and untreated (UT, yellow) scaffolds shown. a) The planned location of the scaffolds on a computer-generated image on the left scapula implanted into the scapula of the sheep. b) Photograph of implanted PEEK scaffolds in left scapula. The two implants below the mesh implants are not relevant for this study.

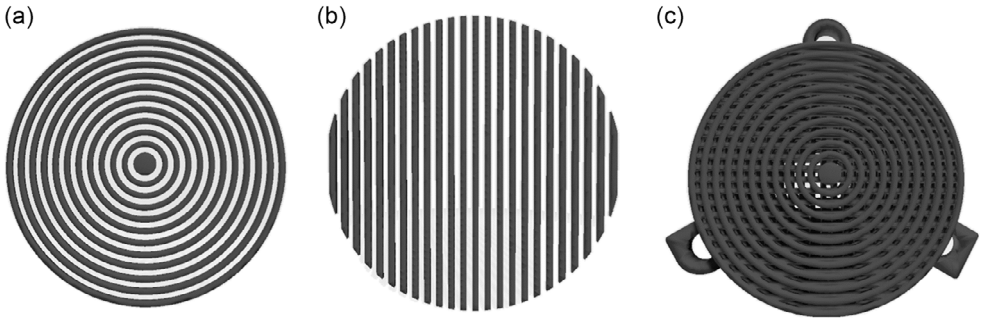

Figure 2. The primary layers for the scaffold comprised concentric rings a), horizontal bars b), stacked to form the structure in c).

Electronik Gmbh, Germany) pulsed DC power supply. The chamber was evacuated to a pressure of 10^{-5}Torr, before nitrogen gas was admitted to the chamber to a pressure of 40 Pa for a treatment time of 20 min and then at 107 Pa for a further 20 min. The different operating pressures were utilized to ensure that the plasma gave sufficient ion dose to the exterior surface at low pressure, but also penetrated the pores of the substrate at the higher pressure.[16,29–31]

2.4. Surgical Procedure and Implant Retrieval

All procedures involving live sheep were performed with approval from the animal ethics committee of the University of Sydney (ethics approval number: 2020/1817). The surgical procedure has been described in detail elsewhere (Kruse et al. 2022).[22] Six male sheep, aged between 7 and 8 years, were separated into two groups (A and B) and underwent surgery under appropriate anesthesia. One sheep was omitted from the analysis in group B due to premature death. The bone of the infraspinous scapula was carefully exposed and two bone defects of 25 mm diameter and of full bone thickness were created using a bone trephine and piezoelectric saw. Each sheep received one PIII treated and one UT mesh implant placed in the lateral and medial infraspinous scapula, respectively (Figure 1b). The muscle tissue surrounding the area was reattached after placement and the wound was closed. The sheep were grouped into group A and group B. In each group, one sheep was euthanized at 8 weeks, one at 10 weeks, and one at 12 weeks postimplantation. In group B, the sheep at 10 weeks was omitted from the study owing to its premature death. To retrieve the mesh implants, the overlying skin, fascia, and muscle were removed and the implants with at least 5 mm of surrounding bone were removed from the scapula by rough circular saw cutting. The mesh implants with surrounding bone were placed in 10% neutral buffered formalin (Livingstone) for tissue fixation. To assess the osteoconduction within the mesh, excess soft tissue has been removed in order to fit the immobilization device for μCT analysis.

2.5. μCT Acquisition and Analysis

The μCT data were acquired on a MILabs UHR (ultrahigh resolution) μCT, using a tube voltage of 50 kVp and a tube current of 0.19 mA, an exposure time of 75 ms, and a step angle of 0.25 degrees for the image acquisition. Images were then reconstructed at one projection per step with a 1 × 1 pixel binning and a spatial resolution of 40 μm. Image analysis was performed in MATLAB2019b using the "dicomread.m" function on the University of Sydney Cluster Network (see acknowledgements). The basic principle of the following method is to use the FePLA as fiducial markers and then using principal component analysis

(PCA)[27] to determine the tilt of the scaffold/stage and determine its coordinates in the CT dataset.

2.5.1. Alignment

FePLA has a much greater HU than the surrounding regular PLA material and air, which makes it easier to locate than the PEEK scaffold.[32] Here, intensity thresholding using the HU was used for the segmentation due to the high contrast/noise ratio. The midpoint of the FePLA ring was located using a center of mass algorithm. The tilt along the z-axis was calculated by taking the corresponding voxel locations in the image as Cartesian coordinates and binning them in a rectangular matrix such that $r_i = [x_i, y_i, z_i]$.The singular values were calculated by making the matrix square by multiplying on the left by the transpose (r_i^{T}). Hence, the covariance matrix $(\mathbf{C})$, was derived

$$\mathbf{C} = \frac{r_i^{\mathrm{T}} r_i}{N-1} \tag{1}$$

We then solved for the singular values of r_i by solving for the singular values of C as follows[33]

$$\mathbf{C} = \mathbf{V}\mathbf{\Lambda}\mathbf{V}^{\mathrm{T}} \tag{2}$$

Here, the eigenvectors $(\mathbf{V} = [\mathbf{v}_1, \mathbf{v}_2, \mathbf{v}_3])$ correspond to the three best lines of best fit drawn through FePLA ring which are the principal components. The principal components correspond to the vector along the axis of the cylinder and the two vectors spanning the axial plane. From the principal component corresponding to the axis of the ring $(\mathbf{v}_{\mathbf{axis}})$, the tilt angle (θ_{t}) was determined from the dot product with the unit vector $(\hat{\mathbf{z}})$

$$\mathbf{v}_{\mathbf{axis}} \cdot \hat{\mathbf{z}} = |\mathbf{v}_{\mathbf{axis}}||\hat{\mathbf{z}}| \cos\theta_{\mathrm{t}} \tag{3}$$

Given that the distance between the midpoint of the FePLA ring and the scaffold is known, the center of the scaffold was located by projecting from the midpoint of the ring (M_{ring}) to the midpoint of the scaffold (M_{scaff}) in n steps along the vector $(\mathbf{v}_{\mathbf{axis}})$, where n is determined from the known distance of the midpoints. From M_{scaff}, the extrema along the z-axis were located using calculations based on the tilt angle (θ_{t}), the radius (R), and the height (h) of the cylindrical scaffold. The total length of the scaffold along the z-axis (l_z) is given as

$$l_z = 2R\sin\theta_{\mathrm{t}} + h\cos\theta_{\mathrm{t}} \tag{4}$$

Hence, the boundary points in the z-axis are found to be $z_{\pm} = M_{\mathrm{scaff}} \pm \frac{l_z}{2}$. The diagrams in **Figure 3**a,b are plotted to visualize the derivation of the quantities in Section 2.5.1.

2.5.2. Obtaining Cross Sections of the Scaffold

For a cylinder tilted at an angle (θ_{t}), the cross section along the imaging Z axis takes the shape of an ellipse, with the lengths of the semimajor $\left(a = \frac{R}{\cos\theta_{\mathrm{t}}}\right)$(green) and semiminor axes $(b = R)$ (yellow), as shown in **Figure 4**. Elliptical cross sections were generated along the axis of the cylinder to the extreme points at l_z. To account for the flat base of the cylinder, two planes were generated at the bases of the tilted cylinders at coordinates

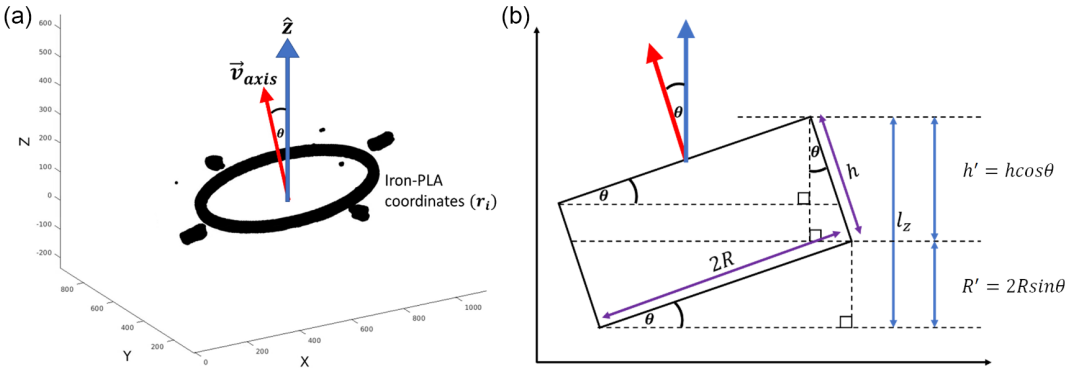

Figure 3. a) Segmented iron-PLA coordinates distributed in Cartesian space (X, Y, and Z are in arbitrary units) with normal vector v_{axis} drawn normal to the plane of the ring. b) The cross section and geometry of the tilted cylindrical scaffold were used to derive the projected height of the scaffold along Z.

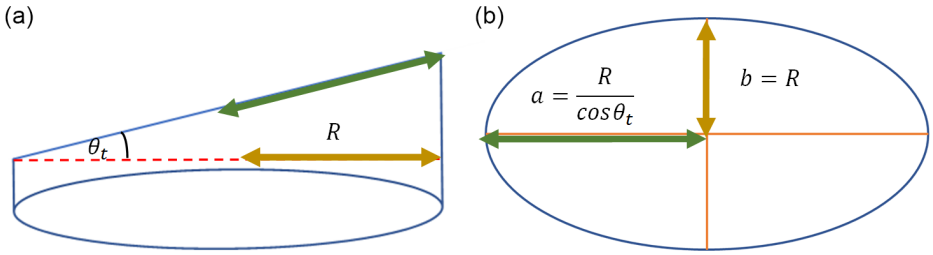

Figure 4. a) A cylinder cut at an arbitrary height at an angle θ_{t} corresponding to the tilt angle. b) Cross section of the cut cylinder with lengths along its semimajor (a) (green) and semiminor (b) (yellow) axes.

(x_l, y_l, z_l) and (x_u, y_u, z_u). The equations of the planes were derived from the principal component $\mathbf{v}_{\text{axis}} = (\mathbf{v}_x, \mathbf{v}_y, \mathbf{v}_z)$ from

$$\mathbf{v}_x(x - x_l) + \mathbf{v}_y(y - y_l) + \mathbf{v}_z(z - z_l) = 0 \tag{5}$$

$$\mathbf{v}_x(x - x_u) + \mathbf{v}_y(y - y_u) + \mathbf{v}_z(z - z_u) = 0 \tag{6}$$

2.5.3. Thresholding

The density and composition of bone is variable, with softer trabecular/cancellous bone possessing a density of $1.0\,\text{g}\,\text{cm}^{-3}$ and cortical bone a density of $1.6–2\,\text{g}\,\text{cm}^{-3}$ as a result of its higher concentration of hydroxyapatite mineral. In the literature, the HU corresponding to the different types of bone are usually given as a range, with cancellous and trabecular bone possessing a HU in the range between 300 and 800 HU and cortical bone with 1000 + HU. Here, solid water and bone calibration phantoms were imaged alongside with HU between 0 and 1200 HU corresponding to various fractions of $CaCO_3$ mineral up to cortical bone. A summary of the calibration values is given in the appendix (A2).

2.5.4. Error Analysis

The segmentation method was first applied first to a nonimplanted scaffold with the final segmented image shown in **Figure 5**a.

The uncertainty in volume (Δ) was calculated from the intersection of volumes between the "known" cylinder ($\mathbf{C}$) and bounding volume ($\mathbf{V}$) given by

$$\Delta = \frac{\mathbf{C} \cap \mathbf{V}}{\mathbf{C}} \tag{7}$$

In Figure 5a, a thresholding range was chosen between −300 and 300 HU, excluding 0 HU to remove the exterior region of the scaffold yielding only the volume of PEEK in this CT dataset, calculated at $952.88\,\text{mm}^3$. Given the volume of PEEK calculated from the slicing software was $954.97\,\text{mm}^3$, giving an uncertainty of 0.2%. For this segmentation, the PEEK and air phase were readily distinguished using intensity thresholding.[34] This method is not as accurate when attempting to segment the tissue in an integrated bone scaffold as there is an additional uncertainty in assigning the correct HU range for the different material phases.

3. Results

There are two quantities of interest: the intensity distribution of HU for the internal volume of the scaffold and its immediate surroundings; the spatial distribution of bone, characterized by a minimum HU, integrated along the z-axis and radially from the symmetry axis of the cylindrical scaffold at its center.

3.1. HU Distribution

The HU distributions of the segmented volumes, corresponding to each set of scaffolds, are shown in **Figure 6**, plotted from a minimum HU of 290. For a CT image, acquired with a polyenergetic X-ray source, a homogenous structure will appear as a Gaussian distribution with a mean HU and standard deviation which will be influenced by neighboring structures and the quality of the CT image. In Figure 5b, only the hard bone and soft tissue are distinguishable, with the other tissue types hidden by noise and scatter. At low HU, there is a high pixel count for all scaffolds, corresponding to the high-tail values from soft tissue. One of the important features in these HU distribution curves is the peaks at higher HU values. These peaks occur between 600 and 650 HU for the PIII treated scaffolds at 12 weeks in Figure 6a,b and between 500 and 600 HU for the UT scaffolds at 12 weeks in Figure 6b. A peak at higher HU indicates the presence of a more attenuating material, most likely bone. For HU values between 290 and 1000, we classify these regions as predominantly bone, with some contributions from soft tissue. In this region, the PIII treated PEEK shows a higher pixel count in each PIII/UT pair, indicating a higher bone count in the interior volume of the scaffold.

The second region of interest is the layer of bone on the external boundary of the scaffold. The HU distribution for a 1 mm external

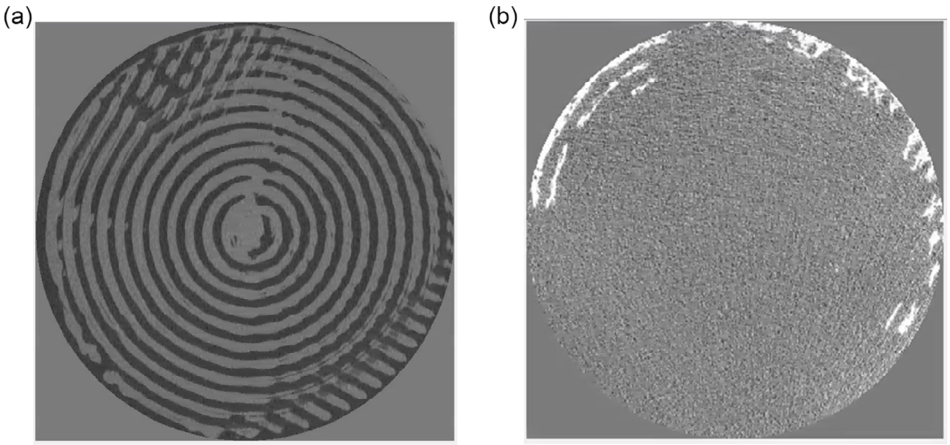

Figure 5. CT slice of a scaffold prior to implantation, segmented using the method described in the text a) CT slice of a PIII treated scaffold, explanted after 12 weeks showing bone mineralization penetrating from the circumference (white) b).

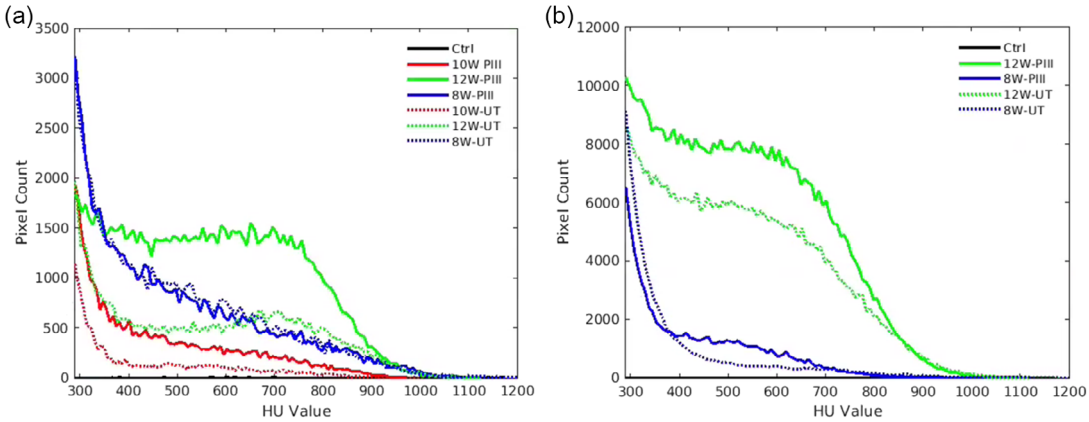

Figure 6. Intensity (pixel count) distribution as a function of HU value for segmented scaffold volumes for sheep in group A a) and group B b), calculated for the interior volume of the scaffolds. The curves with solid lines refer to the PIII treated and the dotted lines to UT. The curves corresponding to nonimplanted scaffolds (Ctrl) are shown as a solid black line. The results for implantation times of 8 W, 10 W, and 12 W (weeks) are plotted in blue, red, and green, respectively. The plots are constrained to HU values greater than 290 and less than 1200 in order to focus primarily on the intensities of bone rather than soft tissue or scaffold material.

shell enclosing the scaffold is shown in **Figure 7**a,b. Here, there is a stark contrast compared to the internal HU distribution, where the UT PEEK now has a higher intensity than the PIII treated implants. The peak between 700 and 900 HU is more prominent in these results compared to the bone in the interior scaffold volume and is also present for all samples. From the distribution curves in Figure 6 and 7, it is clear that there is a greater accumulation of bone outside the scaffold volume in the UT scaffolds, whereas for PIII treated scaffolds there is more bone in the interior.

3.2. Bone Count Along the Axis of the Scaffold

We have defined bone to have a CT value greater than 290 HU. A cumulative summation was performed along the axis of the scaffold, as shown in **Figure 8**.

Figure 8 shows that the PIII treated scaffolds have a higher bone count in the interior of the scaffold compared to the UT scaffolds, except for the implants explanted at 8 weeks in group A, where the intensities are similar. In group A, the biggest change in HU tends to occur toward the middle of the scaffold except for the UT samples at 8 and 12 weeks, which tend to increase toward the deeper end of the scaffold, which is facing interiorly. The radial distributions are shown for the scaffolds in group A and B, respectively, in **Figure 9**a,b.

The entire CT was projected along its axis onto a single slice and then the radial integral was computed from the center of the scaffolds ($r = 0$ mm) up to 1 mm past the boundary of the scaffold ($r = 13$ mm). From Figure 9a,b, there is no significant increase in bone until the scaffold boundary at $r = 12$ mm. For the scaffolds in group A, significant ingrowth is not encountered until $r = 11$ mm. For set B, the onset of bone ingrowth varies between each implant. At the scaffold boundary, we observe a greater count of bone for the PIII treated scaffolds. The ongrowth begins at closer distances to the center of the

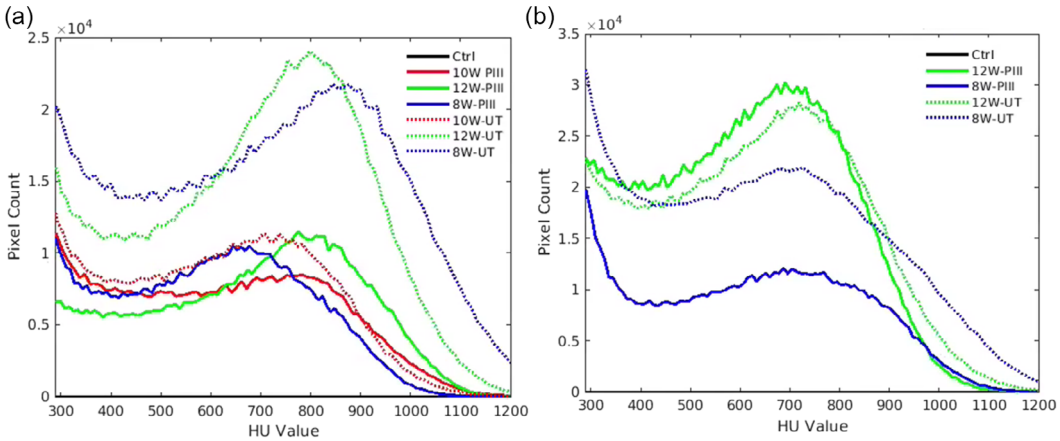

Figure 7. Intensity (pixel count) distribution as a function of HU value for segmented scaffold volumes for sheep in group A a) and group B b), calculated for the exterior volume of the scaffold. The curves with solid lines refer to the PIII treated and the dotted lines refer to UT. The curves corresponding to nonimplanted scaffolds (Ctrl) are shown as a solid black line. The results for implantation times of 8 W, 10 W, and 12 W (weeks) are plotted in blue, red, and green, respectively.

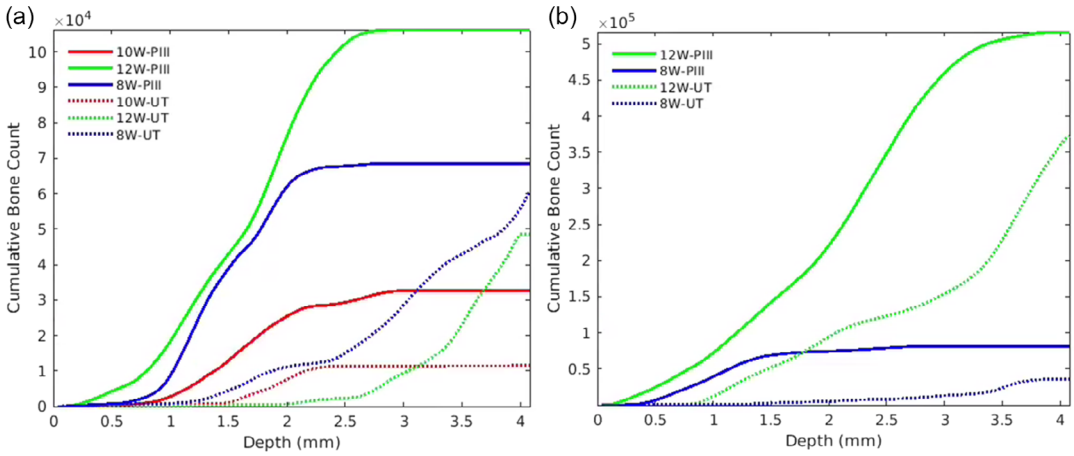

Figure 8. Cumulative bone count (pixel count) using CT values greater than 290 HU plotted as a function of depth along the axis of the scaffold: a) the results from the sheep in group A and b) the results from group B. The curves with solid lines refer to the PIII treated and the dotted lines to UT. The curves corresponding to nonimplanted scaffolds (Ctrl) are shown as a solid black line. The results for implantation times of 8 W, 10 W, and 12 W (weeks) are plotted in blue, red, and green, respectively.

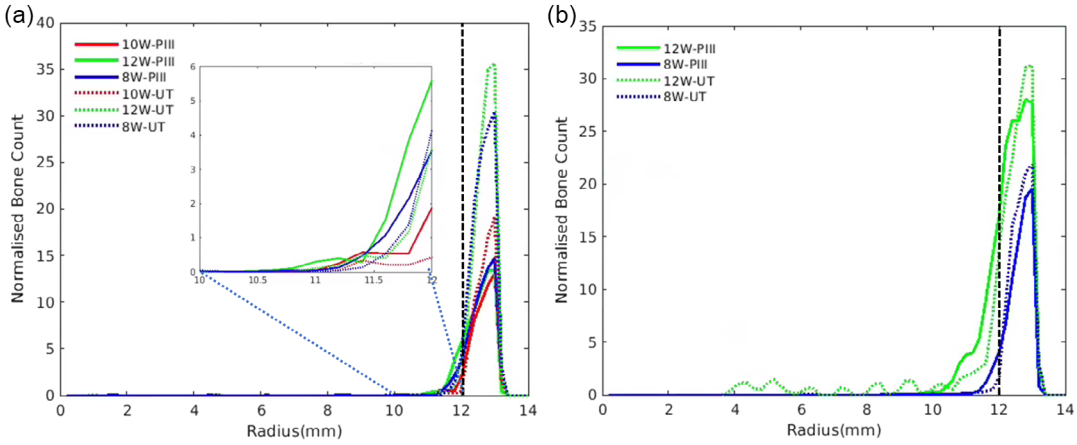

Figure 9. The bone count for the implants in group A a) and Group B b) normalized to unit area, integrated radially from the center of the scaffold to 1 mm past the outer edge of the scaffold. The scaffold boundary is marked at $r = 12$ mm (vertical dashed line). The region at the scaffold boundary in (a) has been enlarged in the inset. The curves with solid lines refer to the PIII treated and the dotted lines to UT. The curves corresponding to nonimplanted scaffolds (Ctrl) are shown as a solid black line. The results for implantation times of 8 W, 10 W, and 12 W (weeks) are plotted in blue, red, and green, respectively. The 12 W UT scaffold in (b) appears to have mineralization in the interior; however, it was found to be ongrowth from the base rather than from the circumference.

scaffolds compared to the UT scaffolds, with the exception of the UT PEEK in set B at 12 weeks, which was confirmed to be growth from the base of the implant and was not penetrating from the outer circumference. Outside the exterior boundary of the scaffold, the bone count is generally higher in the UT scaffolds. The ongrowth on the UT scaffolds also has a steeper increase in bone beyond the boundary compared to the PIII treated scaffolds.

There is a clear difference in the distribution of bone between UT and PIII treated scaffolds around the exterior boundary of the scaffolds where there is a greater intensity in the PIII scaffolds. The greatest ingrowth of bone was observed in the sheep in group B where the scaffold was implanted for 12 weeks. Here, the bone has penetrated the scaffold and is observed to fill the voids of the scaffold. For the PIII scaffold, more bone is concentrated around the circumference inside the scaffold, whereas in the UT case bone was not found in the interior, but only on the exterior surface immediately adjacent to the scapula.

4. Discussion

This μCT study has shown that for UT scaffolds, there is a greater quantity of dense new bone adjacent to, but exterior to, the scaffold. For treated scaffolds, the penetration of dense new bone into the outer edges of the scaffold is greater, although there is somewhat less new bone immediately outside. The percentage of bone by volume for both groups A and B is summarized in **Table 1**.

Table 1. Summary of bone fraction, given as a percentage of the total scaffold volume for groups A and B for all explanted times, for PIII treated (PIII) and UT scaffolds.

Time (weeks)	Volume of bone [%]			
	Group A		Group B	
	PIII	UT	PIII	UT
8	0.22	0.2	0.25	0.035
10	0.11	0.035		
12	0.36	0.16	2.2	0.75

The presence of bone within a scaffold is important because it implies that bone has penetrated the pores, improving the overall mechanical strength of the scaffold.[35,36] In a previous study using 3D printed PEEK implants treated by an identical PIII process. Kruse et al.[22] found that PIII treated scaffolds required a greater torque to liberate them from the surrounding bone. Given that the implants used for the torque test in the previous study were not porous, we expect that in the present case the bone ingrowth into the PIII treated scaffold will result in stronger osseointegration due to both structural interlocking and covalent bonding of biological material to the polymer.[20,21,37] For a

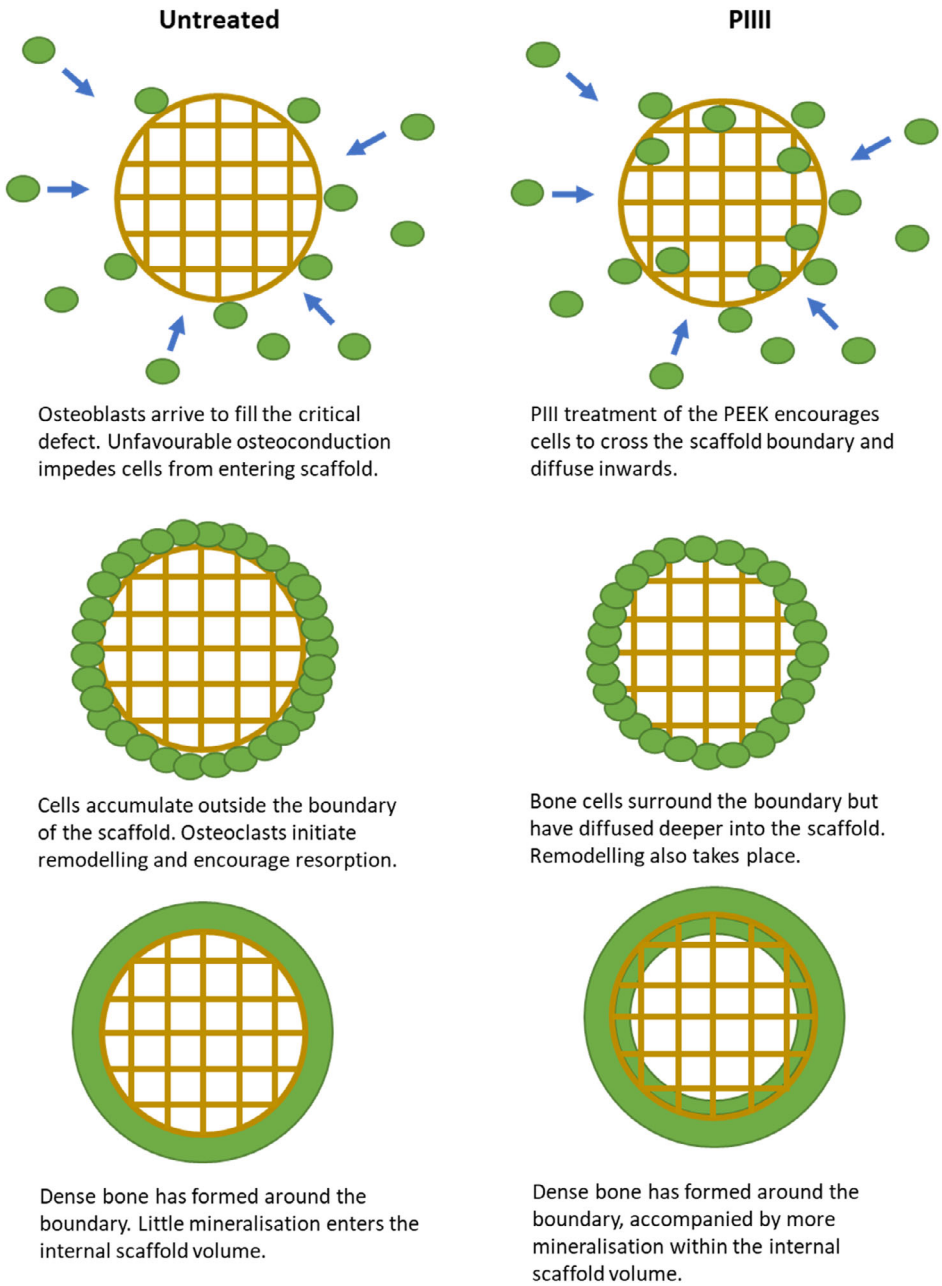

Figure 10. A schematic illustrating the different responses to UT (left) and PIII treated (right) PEEK scaffolds.

connected piece of bone which encloses a porous structure, the increased penetration and surface area from PIII[5,38] create more available sites for the bone to bind more strongly,[39] increasing the resistance to shear forces. The energetic bombardment of the PEEK surfaces with nitrogen ions increases the surface roughness of the material, by introducing various surface textures, etching, densification, or through subsurface gas accumulation.[38] In contrast, the UT scaffolds exhibit a greater bone count on the exterior of the scaffold.

The use of a customized apparatus, incorporating fiducial markers to locate the bounds of the scaffold, was required due to the low contrast between PEEK and soft tissue. This approach allowed us to quantify the osteoconduction into the internal and external volumes of the PEEK scaffold. To accurately quantify the osseointegration as opposed to the osteoconduction, information regarding the anchorage of the bone and the type of tissue would have to be obtained.[40] As the strength of the interface between implant and bone cannot be measured in μCT, only the osteoconduction is assessed. We confirmed that PIII implants have a greater volume of bone present inside the implant adjacent to the interface. This bone is likely to have formed a stronger interface with the surrounding bone.

Regarding the PIII process and the modification of PEEK, the increased hydrophilicity,[14,16,19] the presence of covalent binding sites, and more favorable chemical properties have improved the osteoconduction process. Improved conduction leads to a redistribution of bone mineralization as shown schematically in **Figure 10**. The UT scaffold has an accumulation of bone just outside the outer boundary, while the PIII treatment of the scaffold encourages a greater number of cells to migrate across the boundary, decreasing their number outside the boundary but increasing it in the interior. The increase in bone osteoconduction on PIII treated PEEK surfaces is a likely result of both the improved hydrophilicity and the increased bioactivity arising from the formation of covalent linkages enabled by the radicals from the PIII treatment. The surface analysis has been discussed previously in Kruse et al.[14] The remodeling process by osteoclasts takes place in both cases, but the increased osteoconduction is important in generating a greater amount of mineralized bone in the interior of the PIII treated scaffold.

When comparing the volume of bone and the intensity distribution in HU, for the implants with different explanted times, there is a decrease in intensity in both the HU distribution and bone count when comparing the scaffolds explanted at 8 and 10 weeks. It is suggested that a decrease in bone is the result of bone resorption by osteoclasts.[41,42] The sheep model used in this study is chosen because of the similarities to humans in terms of weight, bone and joint structures, and bone regeneration. Sheep have also been shown to demonstrate similar metabolic rates and bone turnover rates to humans, which make them important for testing bone remodeling in porous scaffolds.[43,44] The remodeling stage of bone turns the softer prebone into more dense bone produced by osteoblasts, which is accompanied by the deposition of hydroxyapatite mineral.[41,42]

This work developed mounting techniques for improving the setup during acquisition of μCT data that enabled the challenging problem of distinguishing PEEK from biologically derived materials. The results show, by comparing bone count at each explantation time of implanted scaffolds from the animals, that PIII treatment provides PEEK with improved osteoconduction properties, enabling osteogenic bone cells to adhere and mineralize more successfully within the interior of the scaffold than was the case for UT implants. The improved osteoconduction results in a greater cumulative bone count along both the longitudinal and radial axes of the scaffolds. The comparison of X-ray scattering power in HU also showed that the bone developed in the PIII treated scaffolds also had a higher density than the bone in the UT scaffolds.

Acknowledgements

Sydney Imaging—Preclinical Core Research Facility—Dr Sophie Trajanovska acknowledge the Charles Perkins Centre for the facilities during the surgery and animal housing. The authors acknowledge the funding from the Australian Government through the Sarcoma Surgical Research Centre at Chris O'Brien Lifehouse. The authors acknowledge the Ian Potter Foundation for the partial funding of the Phenom XL. The authors acknowledge the Cancer Institute New South Wales, Sydney Local Health District, and the Lang Walker Family Foundation. This work was performed during the final year of the corresponding author's Ph.D. candidature, funded by the NHMRC Ideas Grant-GNT1183597 and the University of Sydney Paulette Isabel Jones Completion Scholarship. This work was also performed after this period and funded by the ARC Discovery Grant-DP200101905. The University of Sydney for the Paulette Isable Jones Completion Scholarship for the support to the corresponding author.

Open access publishing facilitated by The University of Sydney, as part of the Wiley - The University of Sydney agreement via the Council of Australian University Librarians.

Conflict of Interest

The authors declare no conflict of interest.

Data Availability Statement

The data that support the findings of this study are available from the corresponding author upon reasonable request.

Keywords

3D printing poly-ether-ether-ketone (PEEK), micro-CT, plasma immersion ion implantation, porous scaffolds, sheep animal trial

Received: September 18, 2022
Revised: December 13, 2022
Published online:

[1] R. A. Durfee, M. Mohammed, H. H. Luu, *Rheumatol. Ther.* **2016**, *3*, 221.
[2] R. Marsell, T. A. Einhorn, *Injury* **2011**, *42*, 551.
[3] A. Tiwari, *J. Clin. Orthop. Trauma* **2012**, *3*, 4.
[4] M. C. Gebhardt, D. I. Flugstad, D. S. Springfield, H. J. Mankin, *Clin. Orthop. Relat. Res.* **1991**, *270*, 181.
[5] C. Reft, R. Alecu, I. J. Das, B. J. Gerbi, P. Keall, E. Lief, B. J. Mijnheer, N. Papanikolaou, C. Sibata, J. Van Dyk, *Med. Phys.* **2003**, *30*, 1162.
[6] D. L. Millis, *Canine Rehabil. Phys. Ther.* **2014**, *7*, 92.
[7] D. Apostu, O. Lucaciu, C. Berce, D. Lucaciu, D. Cosma, *J. Int. Med. Res.* **2018**, *46*, 2104.

[8] O. Akyol, B. Dirican, T. Toklu, H. Eren, T. Olgar, *Dentomaxillofac. Radiol.* **2019**, *48*, 20180267.
[9] A. Niroomand-Rad, R. Razavi, S. Thobejane, K. W. Harter, *Int. J. Radiat. Oncol. Biol. Phys.* **1996**, *34*, 475.
[10] I. J. Das, C. W. Cheng, R. K. Mitra, A. Kassaee, Z. Tochner, L. J. Solin, *Med. Phys.* **2004**, *31*, 3213.
[11] G. A. Katsifis, D. R. McKenzie, R. Hill, M. O'Connor, C. Milross, N. Suchowerska, *Radiat. Phys. Chem.* **2022**, *199*, 110398.
[12] J. B. Jackson III, A. J. Crimaldi, R. Peindl, H. J. Norton, W. E. Anderson, J. C. Patt, *Spine* **2017**, *42*, E1.
[13] Q. Fu, M. Gabriel, F. Schmidt, W. D. Müller, A. D. Schwitalla, *Dent. Mater.* **2021**, *37*, e15.
[14] H. V. Kruse, D. R. McKenzie, J. R. Clark, N. Suchowerska, *Plasma Processes Polym.* **2021**, *18*, 2000219.
[15] E. J. Jansen, R. E. Sladek, H. Bahar, A. Yaffe, M. J. Gijbels, R. Kuijer, S. K. Bulstra, N. A. Guldemond, I. Binderman, L. H. Koole, *Biomaterials* **2005**, *26*, 4423.
[16] G. A. Katsifis, N. Suchowerska, D. R. McKenzie, *Plasma Processes Polym.* **2020**, *17*, 2000113.
[17] R. C. Powles, D. R. McKenzie, N. Fujisawa, D. G. McCulloch, *Diamond Relat. Mater.* **2005**, *14*, 1577.
[18] C. T. Tran, A. Kondyurin, S. L. Hirsh, D. R. McKenzie, M. M. Bilek, *J. R. Soc. Interface* **2012**, *9*, 2923.
[19] F. Awaja, D. V. Bax, S. Zhang, N. James, D. R. McKenzie, *Plasma Processes Polym.* **2012**, *9*, 355.
[20] E. A. Wakelin, G. C. Yeo, D. R. McKenzie, M. M. Bilek, A. S. Weiss, *APL Bioeng.* **2018**, *2*, 026109.
[21] M. M. Bilek, D. R. McKenzie, *Biophys. Rev.* **2010**, *2*, 55.
[22] H. V. Kruse, W. T. Lewin, N. Suchowerska, D. A. Al Maruf, K. Cheng, J. R. Clark, D. R. McKenzie, *Plasma Processes Polym.* **2022**, *19*, e2100244.
[23] Y. Jiang, J. Zhao, E. Y. Liao, R. C. Dai, X. P. Wu, H. K. Genant, *J. Bone Miner. Metab.* **2005**, *23*, 122.
[24] B. S. Müller, Y. M. Ryang, M. Oechsner, M. Düsberg, B. Meyer, S. E. Combs, J. J. Wilkens, *J. Appl. Clin. Med. Phys.* **2020**, *21*, 6.
[25] R. Cancedda, A. Cedola, A. Giuliani, V. Komlev, S. Lagomarsino, M. Mastrogiacomo, F. Peyrin, F. Rustichelli, *Biomaterials* **2007**, *28*, 2505.
[26] M. L. Bouxsein, S. K. Boyd, B. A. Christiansen, R. E. Guldberg, K. J. Jepsen, R. Müller, *J. Bone Miner. Res.* **2010**, *25*, 1468.
[27] D. Nandi, A. S. Ashour, S. Samanta, S. Chakraborty, M. A. Salem, N. Dey, *Int. J. Image Min.* **2015**, *1*, 65.
[28] J. Pelletier, A. Anders, *IEEE Trans. Plasma Sci.* **2005**, *33*, 1944.
[29] C. T. Tran, R. Ganesan, D. R. McKenzie, *Proc. R. Soc. A* **2018**, *474*, 20180263.
[30] M. A. Lieberman, A. J. Lichtenberg, *Principles of Plasma Discharges and Materials Processing*, John Wiley & Sons, New Jersey **2005**.
[31] T. W. Oates, J. Pigott, D. R. McKenzie, M. M. Bilek, *IEEE Trans. Plasma Sci.* **2003**, *31*, 438.
[32] R. Tino, A. Yeo, M. Brandt, M. Leary, T. Kron, *Mater. Des.* **2021**, *199*, 109439.
[33] K. Pearson, *London, Edinburgh, Dublin Philos. Mag. J. Sci.* **1901**, *2*, 559.
[34] N. Sharma, L. M. Aggarwal, *J. Med. Phys.* **2010**, *35*, 3.
[35] G. A. Katsifis, D. R. McKenzie, N. Suchowerska, *J. Compos. Mater.* **2020**, *54*, 2173.
[36] C. N. Kelly, T. Wang, J. Crowley, D. Wills, M. H. Pelletier, E. R. Westrick, S. B. Adams, K. Gall, W. R. Walsh, *Biomaterials* **2021**, *279*, 121206.
[37] M. M. Bilek, D. V. Bax, A. Kondyurin, Y. Yin, N. J. Nosworthy, K. Fisher, A. Waterhouse, A. S. Weiss, C. G. dos Remedios, D. R. McKenzie, *Proc. Natl. Acad. Sci.* **2011**, *108*, 14405.
[38] R. C. Powles, D. R. McKenzie, S. J. Meure, M. V. Swain, N. L. James, *Surf. Coat. Technol.* **2007**, *201*, 7961.
[39] G. R. M. Matos, *J. Maxillofac. Oral Surg.* **2021**, *20*, 1.
[40] T. Albrektsson, C. Johansson, *Eur. Spine J.* **2001**, *10*, S96.
[41] B. Boyce, Z. Yao, L. Xing, *Crit. Rev. Eukaryotic Gene Express.* **2009**, *19*, 171.
[42] E. Kylmaoja, M. Nakamura, J. Tuukkanen, *Curr. Stem Cell Res. Ther.* **2016**, *11*, 626.
[43] D. J. Fagundes, M. O. Taha, *Acta Cir. Bras.* **2004**, *19*, 59.
[44] L. Martini, M. Fini, G. Giavaresi, R. Giardino, *Comp. Med.* **2001**, *51*, 292.